Journal of Solid State Chemistry **166,** 24–41 (2002)
doi:10.1006/jssc.2002.9548, available online at http://www.idealibrary.com on IDEAL®

Complex Polymorphic Behavior and Dielectric Properties of Perovskite-Related $Sr(Sr_{1/3}Nb_{2/3})O_3$

Igor Levin,*[,1] Julia Y. Chan,*[,2] John Henry Scott,* Leonid Farber,†[,3]
Terrell A. Vanderah,* and James E. Maslar*

*National Institute of Standards and Technology, Gaithersburg, Maryland 20899; and †Department of Materials Science and Engineering, University of Pennsylvania, Philadelphia, Pennsylvania

Received November 2, 2001; in revised form February 5, 2002; accepted February 15, 2002

The complex structural behavior of the perovskite-related compound $Sr_4Nb_2O_9$ [$= Sr(Sr_{1/3}Nb_{2/3})O_3$] has been investigated using electron, X-ray, and neutron powder diffraction. Analysis of well-equilibrated specimens annealed at various temperatures indicated that two thermodynamically stable polymorphs occur above and below $T = 1250°C$. The high-temperature (HT) polymorph exhibits an average cubic structure ($Fm\bar{3}m$, $a \approx 2a_c$, where "c" refers to the cubic ~ 4 Å perovskite unit cell) with 1:1 (NaCl-type) partial ordering of Sr^{2+} and Nb^{5+} on the B sites. The low-temperature (LT) phase is monoclinic ($P2_1/n$, $a \approx 6a_c\sqrt{3}$, $b \approx 2a_c\sqrt{2}$, $c \approx a_c\sqrt{6}$, $\beta \approx 90°$) with a distinct, yet unknown, B-cation arrangement. Examination of the HT cubic polymorph using electron diffraction revealed diffuse intensity contours that were consistent with additional local ordering/cluster formation on the sites of the mixed (Sr/Nb) fcc cubic sublattice of the 1:1 ordered B-cation array. Concentration of intensity observed at certain points within the diffuse intensity contours was attributed to superstructure formation. Additionally, refinements of the HT structure using X-ray and neutron powder diffraction data indicated local displacements of both oxygen and A-site Sr atoms which resembled those associated with octahedral tilting. HT-$Sr_4Nb_2O_9$ specimens subsequently annealed at 900°C exhibited remarkably complex chemical and structural behavior: The contours of diffuse intensity were replaced by arrays of sharp superlattice reflections corresponding to at least four distinct metastable superstructures, all derived from the 1:1 B-cation arrangement. Compositional analysis indicated that these phases exhibit Sr/Nb ratios slightly different from 2/1; that is, they are not true polymorphs, but rather a series of structurally distinct phases with compositions near $Sr_4Nb_2O_9$. The metastable superstructures were attributed to ordering of Sr and Nb on the mixed B sites in the 1:1 ordered array, possibly combined with either A-site or oxygen vacancy ordering, depending on the Sr/Nb ratio in the particular phase. The metastable phases transform to the stable LT-$Sr_4Nb_2O_9$ phase upon annealing in the 1100–1200°C temperature range. The dielectric properties of HT- and LT-$Sr_4Nb_2O_9$ were measured by capacitive methods at 1 MHz. HT-$Sr_4Nb_2O_9$ exhibited an ambient permittivity of 40 with a non-monotonic temperature dependence, while that for LT-$Sr_4Nb_2O_9$ was 30 with near-linear temperature dependence. The peculiar dielectric behavior of HT-$Sr_4Nb_2O_9$ was ascribed to the competitive responses of nanodomains having somewhat different structures and compositions. © 2002 Elsevier Science (USA)

1. INTRODUCTION

Complex $A(B'_{1/3}B''_{2/3})O_3$ perovskites display a variety of interesting properties. For example, some of these compounds exhibit relaxor ferroelectric behavior (1), while others feature low dielectric losses and serve as dielectric resonators in wireless communication systems (2, 3). Additionally, non-stoichiometric $A(B'_{1/3+x}B''_{2/3-x})O_{3-\delta}$ perovskites exhibit ionic conductivity (4) and can also absorb significant proton concentrations to become proton conductors (5, 6). The typical crystal–chemical effects observed in these systems include B-cation ordering (7) and/or structural distortion approximated by rotation of nearly rigid $[BO_6]$ octahedra (8, 9); both effects are known to substantially influence dielectric and electrical properties (8, 10). For the stoichiometry $A(B'_{1/3}B''_{2/3})O_3$, two common B-site ordering types have been reported with the ordering vectors $\mathbf{k} = 1/3[111]^*_c$ (1:2 type) and $\mathbf{k} = 1/2[111]^*_c$ (1:1 or NaCl type), respectively (7), where subscript 'c' refers to the ideal cubic ~ 4 Å perovskite unit cell. The 1:2 type ordering corresponds to segregation of the B′ and B″ cations on $\{111\}_c$ planes with the sequence $\{B'B'B'' \ldots\}$, and results in a trigonal $P\bar{3}m1$ structure. The 1:1 type ordering results in a partially ordered structure with alternating $\{111\}_c$ planes occupied exclusively by B″ cations and a disordered mixture of B′ and the remaining B″ cations, respectively. Some

[1]To whom correspondence should be addressed. Fax: 301-975-5334. E-mail: igor.levin@nist.gov.
[2]Present address: Department of Chemistry, Louisiana State University, Baton Rouge, LA 70803.
[3]Present address: Merck & Co., Inc., Pharmaceutical Materials Laboratory, WP78A-31, P.O. Box 4, West Point, PA 19488.

0022-4596/02 $35.00

$A(B'_{1/3}B''_{2/3})O_3$ compounds (9) exhibit polymorphism, with high- (HT) and low-temperature (LT) polymorphs featuring 1:1 (HT) and 1:2 (LT) ordering. Recently, a third metastable polymorph with partial ordering on the "random" sites of the 1:1 ordered array, described by a vector $\mathbf{k} = 1/4[111]^*_c$, was reported for the compound $Ca(Ca_{1/3}Nb_{2/3})O_3$ (9, 10). Following studies of polymorphism in $Ca(Ca_{1/3}Nb_{2/3})O_3$, our attention focused on analogs with cations larger than Ca (i.e., Sr or Ba) possibly occupying both A- and B-sites.

Formation of $Sr(Sr_{1/3}Nb_{2/3})O_3$ (or $Sr_4Nb_2O_9$) with 1:1 ordering of Sr and Nb cations on the B sites (i.e., $Sr[(Sr_{2/3}Nb_{1/3})_{1/2}Nb_{1/2}]O_3$) has been reported in a study of the $SrO–Nb_2O_5$ system ($Fm\bar{3}m$, $a \approx 2a_c$) (11). Earlier reports on this compound alluded to the possibility of partial ordering on the mixed Sr/Nb sites (4, 11), although no evidence for such effects was presented. More recent electron microscopy studies of $Sr_4Nb_2O_9$ (12) revealed complicated diffuse scattering in addition to the fundamental reflections of the 1:1 ordered structure; however, no attempt was made to characterize this scattering. Hervieu *et al.* (11, 13) established that annealing at 1200°C for 72 h results in a transformation of the 1:1 ordered $Sr_4Nb_2O_4$ phase to an orthorhombic polymorph with lattice parameters $a \approx 6a_c\sqrt{3}$, $b \approx 2a_c\sqrt{2}$ and $c \approx a_c\sqrt{6}$. Structural imaging revealed that this polymorph features cubic close packing of $[SrO_3]$ layers, similar to that in perovskite. Annealing of 1:1 ordered $Sr_4Nb_2O_9$ at lower temperature, 900°C, for 72 h produced a collection of yet other superstructures (11), the origin of which was not identified. In the present work, transmission electron microscopy combined with X-ray and neutron powder diffraction was applied to clarify the structural behavior of $Sr_4Nb_2O_9$. Temperature-variable dielectric properties were measured using capacitance methods and correlated with the structural data.

2. EXPERIMENTAL METHODS

Specimens were prepared by solid-state reaction of $SrCO_3$ (99.999%) and Nb_2O_5 (optical grade). Prior to each heat treatment, samples were ground with an agate mortar and pestle for 15 min, pellletized, and placed in an alumina boat on sacrificial powder of the same composition. After an initial overnight calcine at 950°C, multiple 2–4 day heatings with intermediate grinding and re-pelletizing were carried out at 1550°C. Samples were furnace-cooled to 750°C and then air-quenched on the bench top. Specimen colors ranged from white to tan. Typically, five to six heatings were required to attain equilibrium, which was presumed when no further changes could be detected in the details of X-ray power diffraction patterns. Final heat treatments were carried out at various temperatures in the 1600–900°C range followed by air-quenching. Selected specimens were sealed by welding in Pt capsules and quenched in water.

Samples were initially characterized by X-ray powder diffraction (XRPD) using an automated $\theta–2\theta$ Bragg–Brentano diffractometer equipped with incident Soller slits, theta compensating slits, a 0.2 mm receiving slit, a graphite monochromator and a scintillation detector. Data were collected at ambient temperature using Cu$K\alpha$ radiation with a 0.02° (2θ) step size and a 2 s count time per point. Chemical compositions of the specimens were analyzed by X-ray emission energy dispersive spectroscopy (EDS) in a JEOL-840[4] scanning electron microscope (SEM) operated at 10 kV. $SrTiO_3$ (single crystal) and pure Nb were used as standards, while the oxygen content was calculated assuming SrO and Nb_2O_5 stoichiometries. The absolute accuracy of the measurements was estimated using well-characterized specimens of $Sr_2Nb_2O_7$ and $Sr_5Nb_4O_{15}$: the Sr/Nb ratio was systematically underestimated by $\sim 6\%$. The average compositions measured for the $Sr_4Nb_2O_9$ specimens were within this deviation from the corresponding nominal values.

Specimens for transmission electron microscopy (TEM) were prepared by sectioning, grinding, and polishing sintered pellets to a thickness of 30 μm. Final thinning was accomplished in a Gatan precision ion-polishing system (PIPS) at 5 kV until perforation was attained. Some of the specimens were prepared by dispersing powder that had been crushed in acetone onto lacey-carbon-coated copper grids; these specimens were presumed to be free of potential artifacts associated with a bulk TEM specimen preparation, such as reaction with water during grinding/polishing. Because both types of specimens yielded similar results, only those obtained for the bulk specimens will be presented. The specimens were examined using a Phillips 430 TEM microscope operated at 200 kV. *In situ* heating experiments were conducted in the same microscope using a double-tilt Gatan heating stage with a maximum operating temperature of 1000°C. Structural imaging was performed with a JEOL 3010-UHR microscope having point-to-point resolution of 1.7 Å at 300 kV. Phase contrast simulations were conducted using the Bloch waves formalism implemented in the EMS software package (14). Chemical composition in TEM was determined using X-ray emission EDS in the same JEOL 3010-UHR microscope operated at 300 kV. Sr–K and Nb–K X-ray emission lines were used for the analysis. The probe size was about 150 nm in diameter and the acquisition time was 200 s, resulting in a coefficient of variance (CV%) due to counting statistics for the $I_{Sr–K}/I_{Nb–K}$ intensity ratio of less than 2%. The Sr/Nb ratios were calculated from the corresponding $I_{Sr–K}/I_{Nb–K}$ values using the Cliff–Lorimer (15) method. The accuracy of the measurements was estimated using specimens of $Sr_2Nb_2O_7$ compound, for

[4]The use of brand or trade names does not imply endorsement of the product by NIST.

which the measurements (10 points) produced Sr/Nb = 1.04 ± 0.05 (1σ).

X-ray powder diffraction data for Rietveld analysis were collected on a Siemens D500 diffractometer equipped with a focusing Ge incident beam monochromator, sample spinner and a scanning position-sensitive detector (PSD). Cu$K\alpha_1$ radiation was used. The scan range was from 10 to 155° 2Θ. The data collection time was 5 h. Neutron powder diffraction data were collected under ambient conditions using the BT-1 32 detector neutron powder diffractometer at the NIST Center for Neutron Research reactor, NBSR. A Cu(311) monochromator with a 90° take-off angle, $\lambda = 1.5404(2)$ Å, and in-pile collimation of 15 min of arc were used. The samples for neutron powder diffraction were loaded in vanadium can containers. Data were collected over the range of 3–168° 2θ with a step size of 0.05°. The GSAS (16) package was used for Rietveld structural refinement.

Raman scattering was excited nominally at room temperature in a near-backscattering geometry using 785 nm radiation from an argon ion-pumped Ti:sapphire laser. Utilization of 785 nm radiation excitation minimized (but did not eliminate) interference from powder luminescence, which was more intense in the spectra excited with a shorter wavelength radiation. To distinguish features related to Raman scattering from those due to luminescence, Stokes and anti-Stokes Raman spectra were compared. The powders were manually pressed into a stainless-steel powder cup to facilitate specimen handling and spectrum acquisition. Laser radiation was focused onto the powder with a 300 mm focal length cylindrical lens that produced ~ 0.6 mm $\times$ 2 mm rectangular spot with a corresponding power density at the sample of ~ 11 W/cm^2. Scattered radiation was collected and collimated with an achromatic lens located at infinite conjugate ratio. A 785 mm holographic notch filter was placed in the collected collimated radiation. An achromatic lens was used to couple radiation into a 0.46 m imaging spectrograph equipped with a 600 groove/mm grating blazed at 500 nm, and a back-illuminated liquid-nitrogen-cooled charge-coupled device camera system. The instrumental bandpass was ~ 5 cm^{-1}. All spectra were obtained in integration times of 4 s or less.

Dielectric properties were evaluated by capacitance methods at 1 MHz using sintered cylindrical pellets (diameters ~ 8 mm) machined to a height of approximately 1.5 mm. The weak-field complex permittivity was measured using an HP4284A precision LCR meter combined with a Delta Design 9023 temperature chamber. The measurements were conducted in the frequency range from 100 Hz to 1 MHz, while the temperature decreased from 180 to -173°C with a cooling rate of 2°C/min. The uncertainties in permittivites are about 5%, being determined primarily by the uncertainties in specimen dimensions. The pellets exhibited similar bulk densities of $\sim 92\%$, and no correction for porosity was applied to the measured permittivites.

3. RESULTS AND DISCUSSION

3.1. High-temperature $Sr_4Nb_2O_9$: Specimens Cooled from $T > 1250$°C

In accordance with previous investigations (17), X-ray powder diffraction patterns of $Sr_4Nb_2O_9$ specimens cooled from $T > 1250$°C, hereafter denoted as HT specimens, were completely indexable according to the cryolite-type cubic F-centered unit cell with lattice parameters $a = 8.268(2)$ Å $\approx 2a_c$. However, careful examination of the patterns revealed the presence of diffuse intensity in the form of a modulated background (Fig. 1). The details of the background varied slightly between independently prepared specimens of the same composition, but the overall modulated character was reproducible. A similar, though much stronger, modulated background was observed in the neutron diffraction pattern of HT-$Sr_4Nb_2O_9$. Because no second phase was detected in this specimen by either SEM or TEM, this modulated background was attributed to intrinsic structural effects. The higher background intensity observed in the neutron diffraction patterns suggests a strong contribution from the oxygen subcell. Recently, a similar modulated background was observed in the neutron powder diffraction patterns of the perovskite-related $Sr(Sr_{0.4}Ta_{0.6})O_{2.9}$, with 1:1 cryolite-type ordering of Sr and Ta on the B sites (18).

Refinements of the $Fm\bar{3}m$ cryolite-type structural model for $Sr_4Nb_2O_9$ were conducted separately using X-ray and neutron powder diffraction data. The refinements were complicated by very similar scattering cross-sections of Sr and Nb for both X-rays ($\Delta Z = 2$) and neutrons (coherent

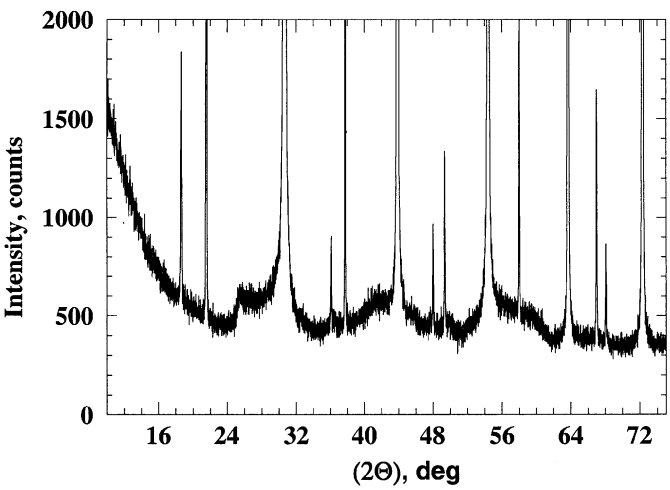

FIG. 1. X-ray powder diffraction pattern of the HT-$Sr_4Nb_2O_9$ specimen. The scale was magnified to demonstrate a modulated background intensity.

TABLE 1
Positional Parameters and Temperature Parameters Refined for the Ideal 1:1 Ordered $Fm\bar{3}m(a = 2a_c)$ $Sr_4Nb_2O_9$ Model Using Separate X-Ray and Neutron Powder Diffraction Data

Atom	Site	x	y	z	Fraction	U_{ISO} ($\times 10^2$ Å^2)
Sr	8c	0.25	0.25	0.25	1	3.05(3)
						3.77(6)
Nb	4a	0	0	0	1	0.37(2)
						0.53(5)
Sr/Nb	4b	0.5	0.5	0.5	0.67/0.33	4.97(5)
						5.64(14)
O	24e	0.2334(3)	0	0	1	7.10(10)
		0.2399(7)				8.17(9)

Note. The upper and the lower entry for the refined structural parameters correspond to the X-ray and neutron datasets, respectively. X ray: $R_{wp} = 11.77\%$, $R_p = 9.05\%$, $R_{F^2} = 7.28\%$, $\chi^2 = 9.87$; neutrons: $R_{wp} = 5.33\%$, $R_p = 5.71\%$, $R_{F^2} = 12.44\%$, $\chi^2 = 6.319$.

TABLE 2
Bond Distances and Bond Valence Sums Calculated for the $Sr_4Nb_2O_9$ Structural Models Presented in Tables 1 and 3

Bond	Bond length (Å)		BVS (v.u.)
	"Ideal model" (Table 1)		
$(Sr_{0.67}Nb_{0.33})$–O	2.080		5.70[a]
Nb–O	1.919		5.87
Sr(A)–O	2.926		1.35
	"Disordered" model (Table 3)		
$(Sr_{0.67}Nb_{0.33})$–O	2.198		4.14
Nb–O	1.975		5.05
Sr(A)–O	2.633×1.5	3.006×1.5	1.74
	2.361×0.75	3.058×0.75	
	2.772×0.75	3.110×0.75	
	2.920×0.75	3.250×0.75	
	2.620×0.75	3.261×0.75	
	2.867×0.75	3.272×0.75	
	2.842×0.75	3.487×0.75	

Note. The atomic positional parameters deduced from the neutron powder diffraction data were assumed.
[a]The ideal BVS value for the mixed Sr/Nb site is equal to 3.00 v.u.

scattering cross-section $b_{Sr} = 6.190$ Å^3, $b_{Nb} = 6.253$ Å^3). As a result, the structure factors of superlattice reflections related to Sr/Nb ordering are determined primarily by oxygen displacements along the B–O bonds; these displacements accommodate the large size mismatch ($\Delta R = 0.54$ Å) between Sr [$R = 1.18$ Å (19), six-fold coordination] and Nb ($R = 0.64$ Å) ions. Consequently, a reliable analysis of site occupancies for Sr and Nb is virtually impossible, but the mixed Sr/Nb (B1) and pure Nb (B2) sites in the 1:1 ordered structure can still be distinguished by the observed B–O bond distances.

The refinements (Table 1) produced rather poor reliability factors of $R_{wp} = 11.77\%$, $R_{F^2} = 7.28\%$ (X ray) and $R_{wp} = 5.33\%$, $R_{F^2} = 12.44\%$ (neutrons); additionally, abnormally large values of temperature (displacement) parameters were obtained for all ions except niobium on the B2 sites (Table 1).[5] Similar temperature parameters were reported for $Sr(Sr_{0.4}Ta_{0.6})O_{2.9}$ (18). Bond valence sum (BVS) calculations (20) using refined Sr–O bond distances (Table 2) indicated an abnormally large residual tension about Sr at the A sites ($BVS_{meas} = 1.35$ v.u., $BVS_{ideal} = 2$ v.u.), and compression ($BVS_{meas} = 5.7$ v.u., $BVS_{ideal} = 3.00$ v.u.) about the mixed B1 sites.

The tolerance factor estimated for the $Sr_4Nb_2O_9$, assuming random occupancy of B sites by Sr and Nb, is equal to 0.90 and, therefore, octahedral tilting was expected to satisfy bonding requirements of Sr cations on the A sites. Long-range correlated octahedral tilting, if present in the structure, would produce a distortion of the ideal cubic lattice; however, no splitting or asymmetry of the cubic reflections was detected in the X-ray powder diffraction pattern up to $2\Theta = 155°$. Therefore, the abnormally large temperature parameters for both the oxygen and the A-site Sr atoms can be attributed to their displacements (from the special positions) which are necessary to achieve a stable (ideal BVS) A-site environment. The modulated nature of the diffuse background suggests that these displacements may exhibit short-range correlations; however, crystallographic refinements using Bragg reflections can treat such displacements as disordered only.

[5]The background was modeled using GSAS type 6 (8 coefficients) function and Chebyschev polynomial (18 coefficients) for the X-ray and neutron data, respectively.

TABLE 3
Positional and Temperature Parameters Refined for the 1:1 Ordered $Fm\bar{3}m$ $(a = 2a_c)$ $Sr_4Nb_2O_9$ Model Using Separate X-Ray (Upper Entries) and Neutron (Lower Entries) Powder Diffraction Data

Atom	Site	x	y	z	Occupancy	U_{ISO} ($\times 10^2$ Å^2)
Sr	32f	0.2338(1)	0.2338(1)	0.2338(1)	0.25	1.07(2)
		0.2295(3)	0.2295(3)	0.2295(3)		0.38(12)
Nb	4a	0	0	0	1	0.45(1)
						2.22(8)
Nb/Sr	4b	0.5	0.5	0.5	0.333/0.67	4.95(4)
						4.41(13)
O	96k	0.2321	0.0324	0.03243	0.25	1.60(3)
	192l	0.2371	0.03360	−0.0216	0.125	7.22[a]

Note. X ray: $R_{wp} = 10.58\%$, $R_p = 8.18\%$, $R_{F^2} = 6.36\%$, $\chi^2 = 7.968$; neutrons: $R_{wp} = 3.81\%$, $R_p = 4.62\%$, $R_{F^2} = 8.48\%$, $\chi^2 = 3.26$.
[a]$U_{11} = 0.026(1)$ Å^2, $U_{22} = 0.10(1)$ Å^2, $U_{33} = 0.091(6)$ Å^2, $U_{12} = 0.041(6)$ Å^2, $U_{13} = -0.063(40)$ Å^2, $U_{23} = 0.012(5)$ Å^2.

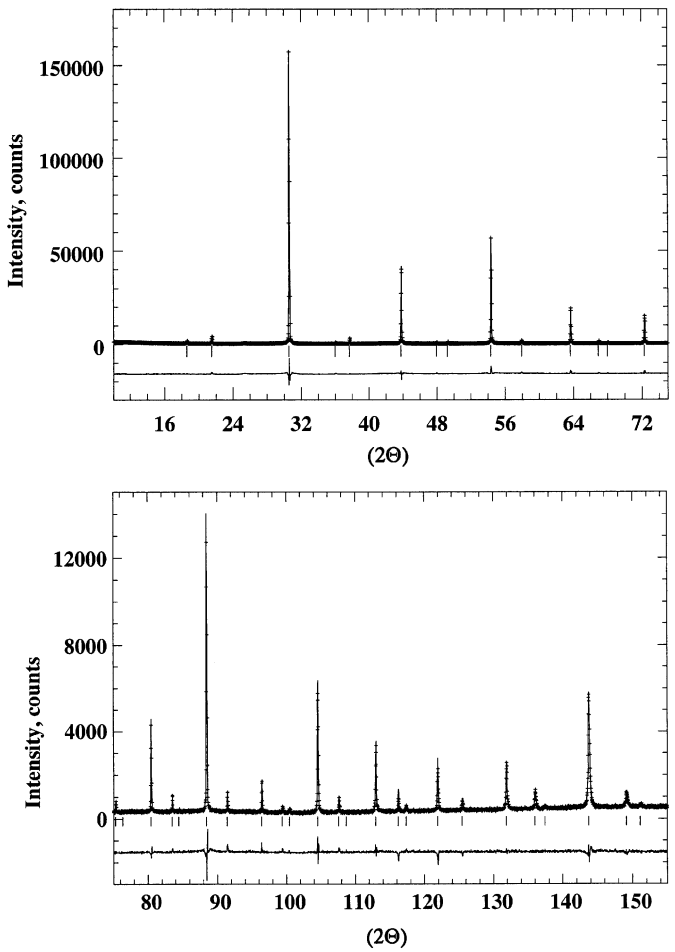

FIG. 2. (Upper) Experimental (crosses) and calculated (line) X-ray powder diffraction profiles of $Sr(Sr_{1/3}Nb_{2/3})O_3$ annealed at 1550°C. The calculated profile corresponds to the model described in Table 3. (Lower) Residual.

The fit was improved ($R_{wp} = 11.7\%$, $R_{F^2} = 6.43\%$ for X-ray, and $R_{wp} = 3.81\%$, $R_{F^2} = 8.48\%$ for neutrons) by introducing positional disorder for the A-site Sr and the oxygen ions (Table 3, Figs. 2 and 3). For the X-ray diffraction data (Table 3), the displacement parameters of the Sr and O were significantly reduced in the disordered model but those of Sr/Nb on B1 sites were still much higher than normal. However, for the neutrons, Table 3, the oxygen displacement parameters remained abnormally large even with the oxygen ions disordered on the general 192*l* site. Oxygen displacements appeared strongly anisotropic with the largest components directed normal to B–O bonds, which is similar to the displacements associated with octahedral tilting. As expected, displacements of the oxygen and A-site Sr ions from their special positions significantly decreased residual bond strain at all sites (Table 2), although the BVS for the mixed B1 sites still remained abnormally large (4.14 v.u. versus the ideal value of 3.00 v.u.). The abnormal temperature parameters for the B1 sites likely reflect some displacements of the Sr/Nb cations; however, no reduction in the temperature parameters was obtained by introducing positional disorder on these sites.

Electron diffraction patterns from a single grain of HT-$Sr_4Nb_2O_9$ consistently exhibited extended diffuse scattering in addition to the fundamental reflections described by the cubic double-perovskite unit cell (Fig. 4). No significant difference in diffuse scattering was observed between water-quenched and slowly cooled specimens. *In situ* heating of these specimens in the microscope with a 3 h exposure at 950°C did not produce any visible changes in the diffraction patterns. Examination of different sections of the reciprocal lattice confirmed that the diffuse intensity concentrates on a surface (Fig. 5), which resembles that described by

$$\cos \pi h + \cos \pi k + \cos \pi l - \gamma(\cos \pi h \cos \pi k \cos \pi l) = 0, \quad [1]$$

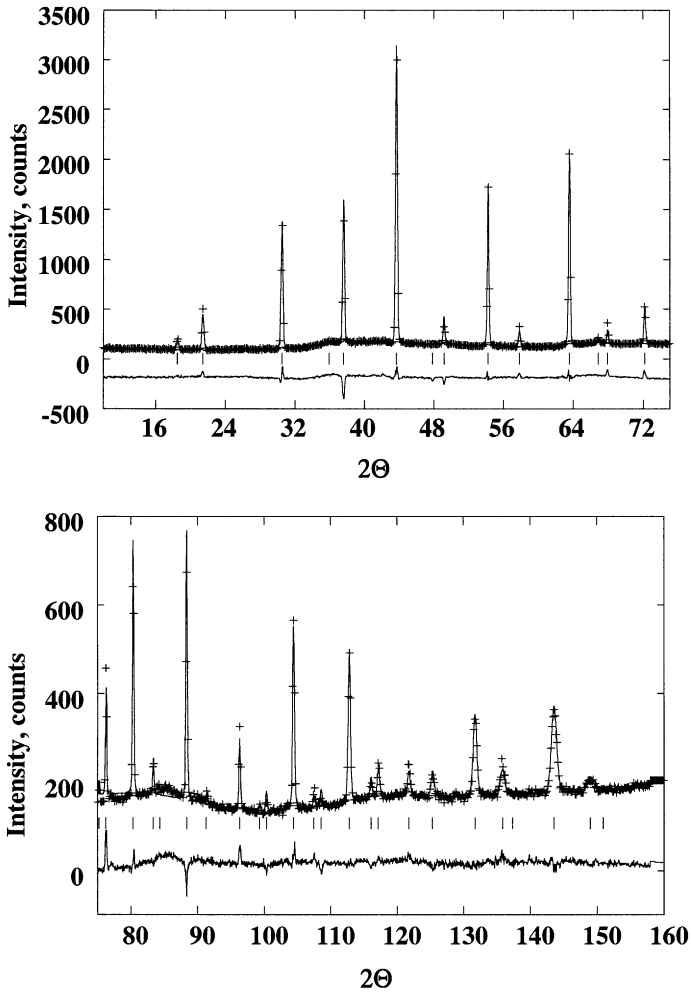

FIG. 3. (Upper) Experimental (crosses) and calculated (line) neutron powder diffraction profiles of $Sr(Sr_{1/3}Nb_{2/3})O_3$ annealed at 1550°C. The calculated profile corresponds to the model described in Table 3. The contribution of modulated background in the experimental pattern is much stronger compared to the X-ray diffraction pattern in Fig. 1. (Lower) Residual.

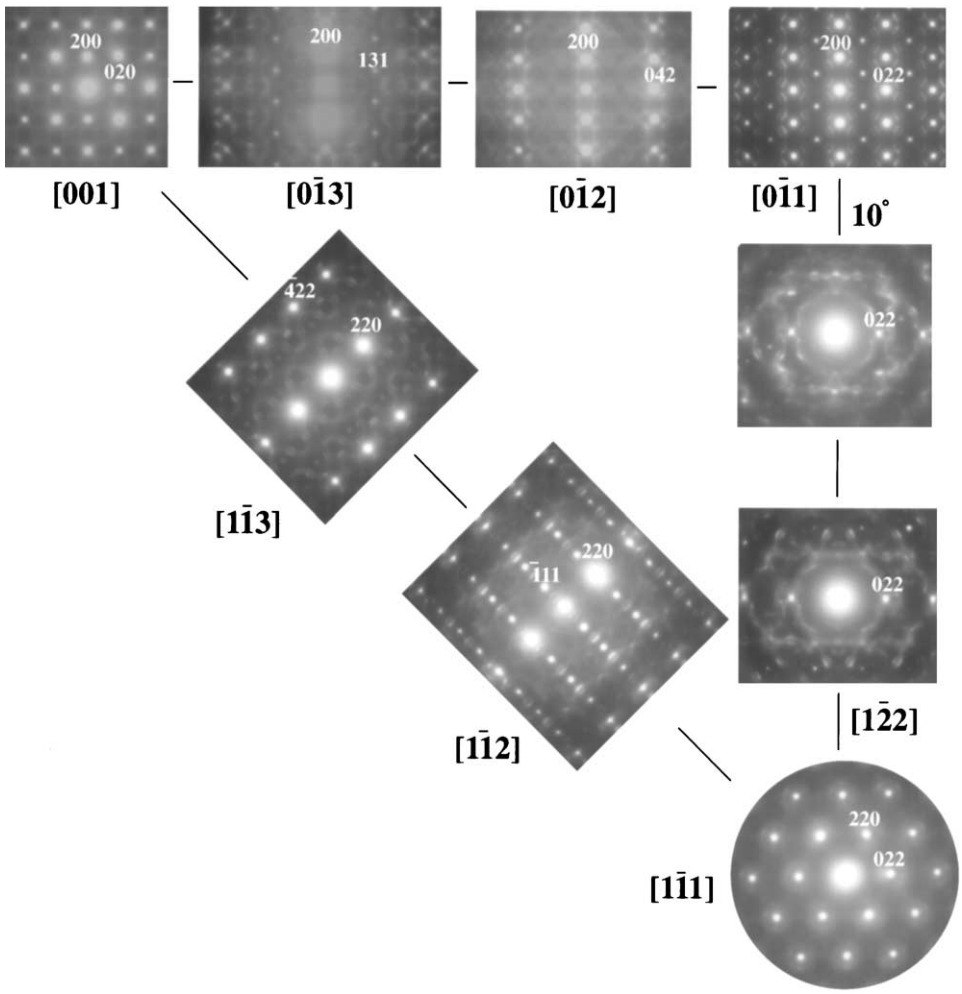

FIG. 4. Set of selected area electron diffraction patterns from a single grain of an $Sr(Sr_{1/3}Nb_{2/3})O_3$ sample annealed at 1550°C. The fundamental reflections are indexed according to the cubic $Fm\bar{3}m$ structure with $a \approx 2a_c$. All patterns reveal extended diffuse scattering with a condensation of diffuse intensity at certain points of reciprocal space.

where h, k and l are coordinates of reciprocal space and γ is a fixed parameter. This equation represents a manifold of surfaces constructed from the two basic surfaces:

$$\cos \pi h + \cos \pi k + \cos \pi l = 0, \qquad [2a]$$

$$\cos \pi h \cos \pi k \cos \pi l = 0. \qquad [2b]$$

The ordering state associated with diffuse intensity located either on a line or on a surface has been termed a "transition state" (21) to distinguish it from short-range order, with a three-dimensional distribution of diffuse intensity, and from long-range order, with diffuse intensity concentrated in superstructure reflections. A so-called "cluster model" was developed (21, 22) which describes a "transition state" built of atomic clusters of a specific polyhedral type, satisfying a linear relationship between the occupational operators on the cluster sites; for ionic compounds, this model is a direct extension of the Pauling electrostatic valence rule (23). Surfaces of diffuse intensity similar to that described by Eq. [1] have been observed in some transition metal carbides (VC_{1-x}, TiC_{1-x}, NbC_{1-x}), nitrides (TiN_{1-x}) (22, 24) and oxides ($LiFeO_2$) (23) having an NaCl-type structure. Diffuse scattering in these systems was attributed to ordering of species sharing the same fcc sublattice (i.e., carbon atoms and vacancies in carbides, or Li and Fe in $LiFeO_2$), accompanied by formation of octahedral and cubic clusters of these species in real space (21, 22). Octahedral and cubic clusters give rise to diffuse intensity surfaces described by Eqs. [2a] and [2b], respectively. Despite general similarity, the actual shape of the diffuse intensity surface for the HT-$Sr(Sr_{1/3}Nb_{2/3})O_3$ specimens deviates from that shown in Fig. 4. For example, additional streaks of diffuse intensity along the $\langle 110 \rangle$ directions are observed in the $\langle 001 \rangle$ reciprocal lattice sections, plus a visible condensation of diffuse

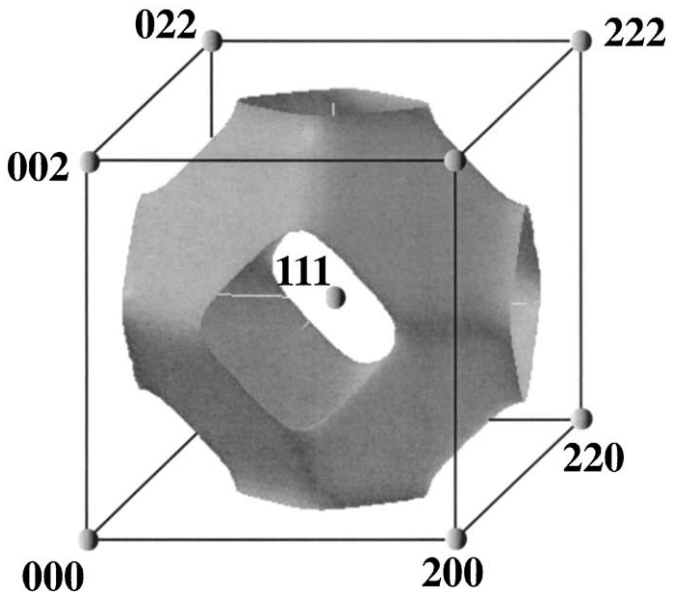

FIG. 5. Surface described by Eq. [1] with $\gamma = 3$. This surface describes approximately the locus of diffuse intensity observed in the SAD patterns shown in Fig. 3. The surface is triply periodic in reciprocal space. The reciprocal lattice of the $Fm\bar{3}m$ structure is also shown in the figure.

intensity at specific points in reciprocal space which reflects development of a nanometer-scale superstructure. Nevertheless, the overall shape of the diffuse intensity surface in the HT-$Sr_4Nb_2O_9$ is largely accounted for by formation of octahedral (predominantly) and cubic clusters on the mixed B1 sites of the NaCl-type ordered cation array. Examples of two distinct B1-site octahedral clusters with stoichiometric Sr/Nb ratios of 2 are illustrated in Fig. 6. A single cubic cluster cannot accommodate an Sr/Nb ratio of 2 and, therefore, several cubic clusters with appropriate abundancies are required to satisfy the average stoichiometry.

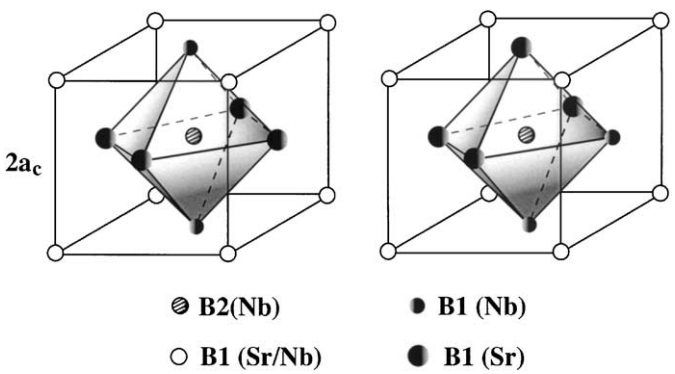

FIG. 6. Octahedral clusters on the B1 sites having stoichiometric Sr/Nb ratio of 2:1. B2 sites on edges of the cube have been omitted for clarity.

The local ordering responsible for the diffuse intensity can be revealed using structural imaging in a high-resolution TEM. Figure 7 shows a typical structural image from the through-focus series recorded for a single $Sr_4Nb_2O_9$ grain in the $[110]_c$ zone axis orientation. The average contrast in the image is consistent with the double-perovskite F-centered cubic unit cell, while the presence of a modulation in the image is evident from the diffuse scattering observed in the corresponding fast Fourier transform (FFT) pattern. Comparison of the experimental image with the contrast, simulated using the refined $Sr_4Nb_2O_9$ model (Table 1) for a broad range of thickness–defocus permutations, indicated that the bright spots in the image correspond to the B-site columns with the brightest spots representing the B1 sites. The effect of the modulation on the contrast as enhanced by applying a Fourier filter to the experimental image with the diffuse scattering and the four fundamental reflections (encircled in Fig. 7b) participating in the inverse Fourier transform; the fundamental reflections were weighed by a factor $w = 0.2$. The intensity modulation in the resulting image clearly displays local order, but no visible long-range superlattice periodicity is observed.

Computer simulations of structural images indicated that purely occupational 1:1 ordering of Sr and Nb contributes little to the phase contrast. The contrast due to 1:1 ordering is determined primarily by the oxygen displacements along the B–O bonds. Therefore, interpretation of contrast variations in terms of the B-site occupancies necessarily requires accurate modeling of oxygen displacements associated with specific B-cation distributions. Phase contrast interpretation is further complicated by the possible interference of oxygen displacements not related to B-cation ordering (for example, octahedral tilting). Thus, an unambiguous assignment of the observed contrast to the specific B-cation arrangement is not possible.

The combined X-ray, neutron and electron diffraction techniques indicate that the local room-temperature structure of what has been commonly referred to as the "$Sr_4Nb_2O_9$ high-temperature polymorph" (4–6, 11, 12) deviates significantly from the ideal cubic model with partial NaCl-type ordering of Sr and Nb cations on the B sites. X-ray and neutron diffraction data indicate that both A-site Sr and oxygen atoms undergo displacements which resemble those associated with octahedral tilting; most likely, the displacements exhibit short-range correlations, but those could not be ascertained by crystallographic refinements. The shape of the diffuse intensity surface identified by electron diffraction suggests local ordering on the mixed B1 sites of the average 1:1 ordered structure. The observed concentration of diffuse intensity in superlattice reflections suggests that the specimen is composed of superstructure nanodomains. The results from the HT specimens are inconclusive with regard to the number of superstructures in the specimen.

3.2. *Low-temperature $Sr_4Nb_2O_9$ Polymorph: Specimens Annealed at 1100–1200°C*

Annealing the HT specimens between 1100 and 1200°C resulted in a phase transition to a structure with an orthorhombic unit cell and lattice parameters $a = 42.8738(2)$ Å $\approx 6a_c\sqrt{3}$, $b = 11.6841(6)$ Å $\approx 2a_c\sqrt{2}$ and $c = 10.1859(5)$ Å $\approx a_c\sqrt{6}$ (Fig. 8). This structure, hereafter denoted as LT-$Sr_4Nb_2O_9$ phase, is similar to one reported by Hervieu *et al.* (13).

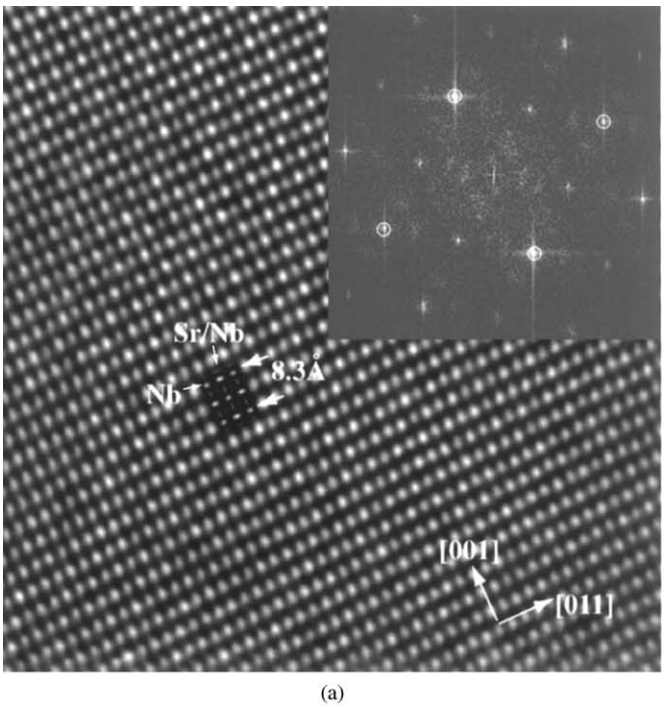

(a)

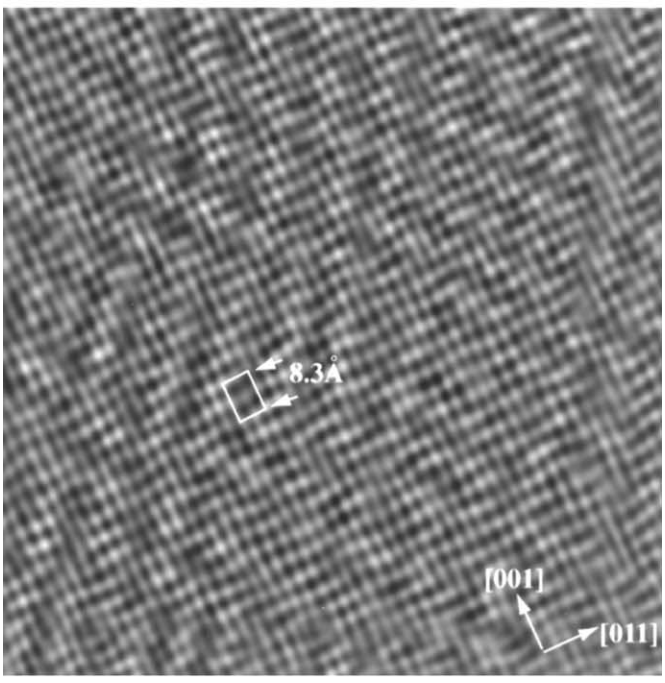

(b)

The HT → LT transformation was reversible with the transition temperature located in the range 1200–1250°C. The transition exhibited slow temperature-activated kinetics. In particular, the transformation was still incomplete after annealing at 1100°C for 72 h or after annealing at 1200°C for 35 h. In addition to the LT phase, the partially transformed HT specimens treated directly at 1100°C contained several metastable phases which will be discussed in the next section. In contrast, the HT specimens annealed at 1200°C did not contain any of these metastable phases, while some untransformed grains of HT phase, featuring diffuse scattering, were occasionally observed. Thus, the HT → (metastable phases) transition temperature is located between 1100 and 1200°C.

For the LT-$Sr_4Nb_2O_9$ phase two possible orthorhombic space groups, *Pmna* (No. 53) and *P2na* (No. 30), have been proposed; both groups have similar reflection conditions $h0l$: $h + l = 2n$, $hk0$: $h = 2n$, $h00$: $h = 2n$, $00l$: $l = 2n$ (27). The present study (Fig. 8) confirmed all, but $hk0$, reflection conditions: the $hk0$ reflections with $h = 2n$ were observable both in the diffraction patterns from a single orientational variant and in FFT patterns from the structural images. Consequently, we assumed that no *a*-glide symmetry plane perpendicular to the *c*-axis is present in the structure. Additionally, the $k = 2n$ reflection condition was observed for the $0k0$ reflections by tilting the specimen away from the zone axis orientation. This reflection condition suggests the presence of 2_1 axes parallel to the *b*-axis which is inconsistent with both *Pmna* and *P2na* space groups. Structural imaging along the *b*-axis (Fig. 9a) revealed a cubic close-packed sequence of atomic layers along the $[111]_c$ direction with 18 layers (18L) in the unit cell. Such a structure does

FIG. 7. (a) Structural image of the HT-$Sr_4Nb_2O_9$ specimen recorded in the $\langle 110\rangle_c$ zone axis orientation slightly below Scherzer defocus ($\Delta f = -36$ nm for the JEOL-3010 UHR microscope). The diffraction pattern from this crystal is identical to that shown in Fig. 3. The FFT of the image (shown as an inset) reveals diffuse scattering similar to that observed in the SAD pattern. The average contrast exhibits periodicity corresponding to the $\langle 110\rangle$ projection of the $Fm\bar{3}m$ cubic structure with $a = 2a_c = 8.3$ Å. The computer-simulated image using the refined model (Table 1) is superimposed; the defocus and thickness for the calculated image are $\Delta f = -64$ nm and $t = 22$ nm. The bright spots in the image correspond to the B-cation columns, with the brightest spots representing larger Sr-rich B1 sites. (b) The same image Fourier-filtered using diffuse scattering and the four fundamental reflections (encircled in the FFT pattern); the intensities of fundamental reflections were weighted by a factor $w = 0.2$ to enhance the contribution of diffuse scattering. The image clearly features modulation of intensities of black and white spots in the image. The presence of a short-range correlation of this intensity modulation is evident, but no long-range superlattice periodicity is observed. According to the image simulations, the contrast variations arise primarily from the oxygen displacements along the B–O bonds.

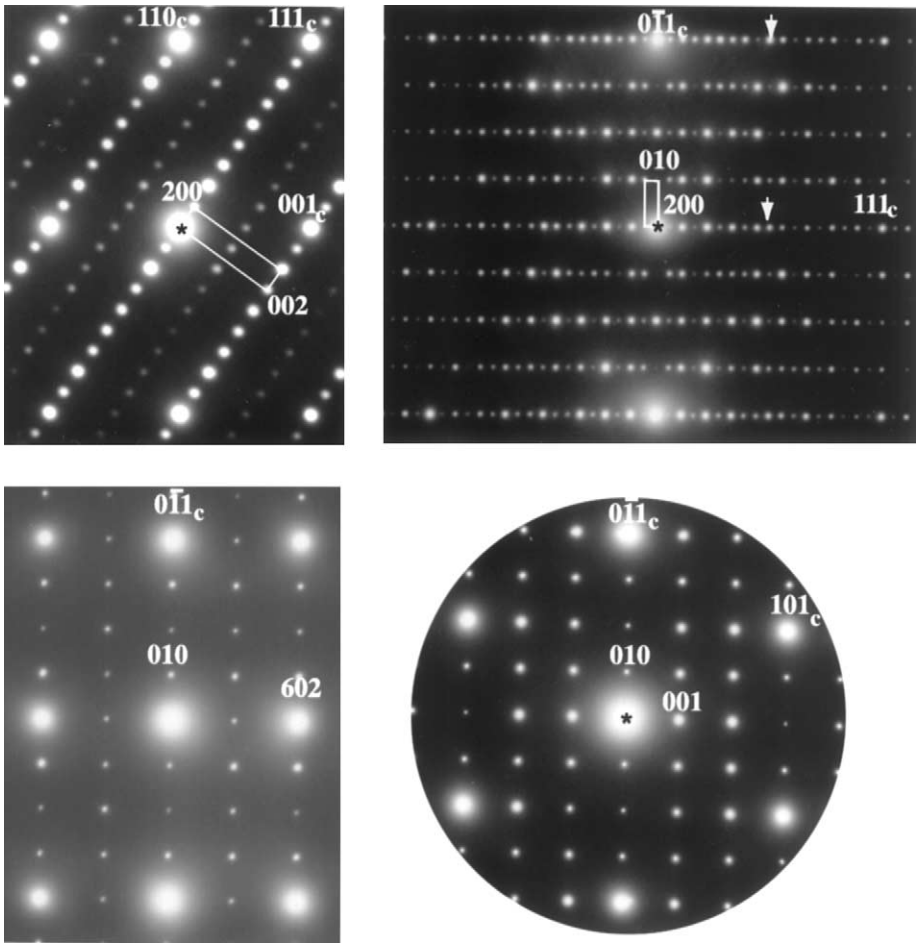

FIG. 8. Representative electron diffraction pattern from the single domain of the LT-$Sr_4Nb_2O_9$ polymorph. The patterns are indexed with a pseudo-orthorhombic unit cell with lattice parameters $a \approx 6\sqrt{3}a_c$, $b \approx 2\sqrt{2}a_c$, $c \approx \sqrt{6}a_c$ and $\beta \approx 90^\circ$. The fundamental reflections are additionally indexed according to the cubic perovskite unit cell with $a = a_c$.

not possess mirror planes perpendicular to the stacking direction (a-axis of the orthorhombic unit cell), and, therefore, the space group is likely to be monoclinic $P2_1/n$, (No. 14, setting 2, b the unique axis). The symmetry of the phase contrast in the [001] structural image (Fig. 9b) is close to $p2gg$ (27) expected for the $P2_1/n$ space group; observed deviations from ideal symmetry were attributed to a slight misorientation of the zone axis with respect to the electron beam.

In contrast to the HT structure, the stable LT-$Sr_4Nb_2O_9$ polymorph does not exhibit alteration of Nb- and Sr/Nb-occupied $\{111\}_c$ cation planes, as inferred from the absence of $\mathbf{k} = 1/2[111]^*_c$ reflections along the stacking direction. The phase contrast observed in the [010] orientation can be interpreted by assuming that the rows of alternating white/dark spots parallel to the $\{111\}$ planes which contain the darkest spots (Fig. 9) correspond to the Sr-occupied B-site $\{111\}_c$ planes. The interpretation implies the following sequence for nine $\{111\}_c$ cation planes: (SrNbNbNbSrSrNbNbNbSr…) which is consistent with the Nb/Sr = 2 ratio on the B sites. The contrast observed in the [001] orientation is also consistent with this interpretation. A combination of such ordering with anti-phase octahedral tilting (which requires doubling of the ideal perovskite unit cell) would account for the observed 18L periodicity. However, the $b \approx a_c\sqrt{2}$ lattice parameter in the resulting unit cell is only a half of that experimentally observed; that is, the actual structure must exhibit some extra ordering in the $\{111\}$ planes. Conceivably, a separation of Sr and Nb into different $\{111\}$ B-cation planes, suggested by the image, is incomplete, giving rise to an additional in-plane ordering of these cations. Unfortunately, weak contrast between Sr and Nb, combined with the large unit cell volume of ~ 4600 Å^3 and monoclinic symmetry, make structural solution of this phase extremely difficult.

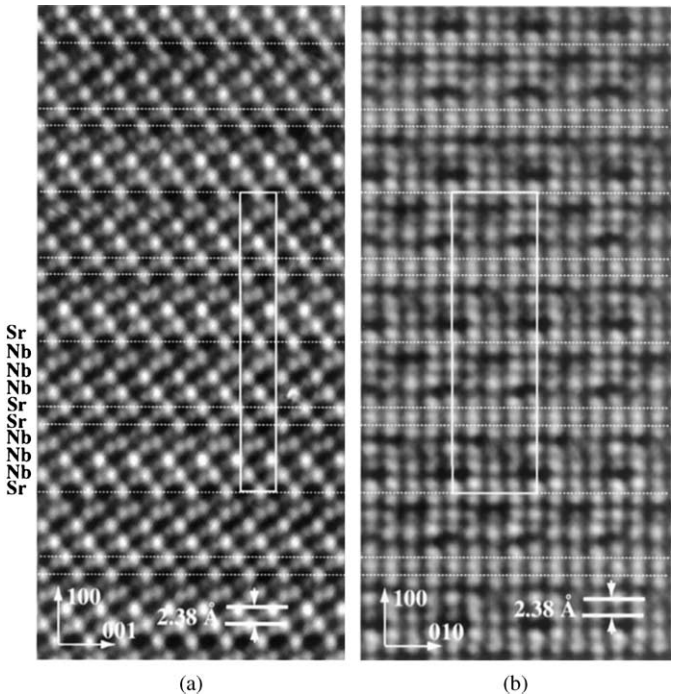

FIG. 9. Structural images of the LT-$Sr_4Nb_2O_9$ polymorph in the (a) [010] and (b) [001] zone axis orientations. The [010]-image reflects a cubic close-packed stacking of the atomic layers along the $[100] \| [111]_c$ direction. The image features a nine-layer (9L) periodicity along the [100] direction as the contribution of 110 reflections to the phase contrast for the thin areas is very weak; the complete 18L unit cell is outlined in the image. The rows of alternating bright/dark spots parallel to the (100) plane and containing the darkest spots in the image were attributed to the Sr-rich B-cation planes. In this interpretation, the bright spots in the image correspond to the tunnels of low electron density between the octahedra.

3.3. *Metastable Phases: Specimens Annealed at 900°C*

Annealing the HT-$Sr_4Nb_2O_9$ specimens at 900°C for 72 h produced complicated arrays of superlattice reflections in the electron diffraction patterns (Fig. 10); no further changes were detected after prolonged annealing for 500 h.[6] Some of the patterns were similar to those reported by Hervieu *et al.* (11). Dark-field imaging using superlattice reflections revealed a multi-domain microstructure with domain sizes of about 50–100 mm (Fig. 10). Electron micodiffraction combined with Fourier analysis of structural images confirmed that these domains represent different superstructures, denoted as IC, T, M and R (Table 4); the chemical compositions and structural features of these phases are discussed below. The IC structure was dominant (> 50 vol%), while both *M* and *R* domains had relatively similar volume fractions, and the T phase was present only in minor quantities. The specimens exhibited clustering of domains with similar structures, rather than a random mixture of domains types.

Compositional analysis of these superstructures was conducted in TEM using a stationary electron probe (about 150 nm in diameter). In this approach, electron microdiffraction was used to monitor crystal structure of the analyzed area during the EDS spectra acquisition. Compositional measurements produced similar Sr/Nb

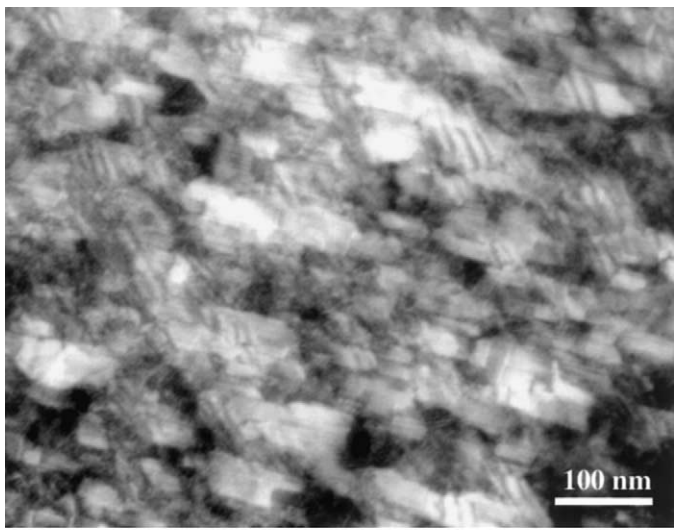

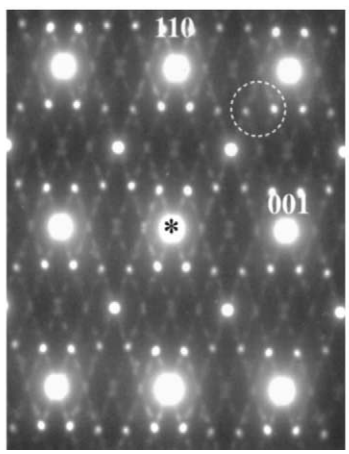

FIG. 10. Representative ⟨110⟩ zone axis electron diffraction pattern from $Sr_4Nb_2O_9$ annealed at 900°C for 500 h. The fundamental reflections were indexed according to a cubic double-perovskite unit cell ($Fm\bar{3}m$). Complex arrays of sharp superlattice reflections are observed. A multi-beam dark-field image, formed with several superlattice reflections (circled in the pattern) strongly excited near the ⟨110⟩ zone axis orientation, features collection of domains, 50–100 nm in size (top).

[6]X-ray powder diffraction patterns from these specimens featured weak broad superlattice reflections, as well as the splitting of the fundamental cubic reflections.

TABLE 4
Structural and Compositional Parameters of the Metastable Phases Identified in the 900°C-Annealed Specimens

Phase	Unit cell	Lattice parameters/ modulation vector	Sr/Nb ratio
IC	Incommensurate	$\mathbf{q} = (\frac{1}{4}\text{-}z)\langle 221\rangle_c^a$, $z = 0.009$	> 2
T[a]	Pseudotetragonal	$\mathbf{q} = \frac{1}{4}\langle 221\rangle_c^a$, $a = 2a_c\sqrt{2}$, $b = 2a_c\sqrt{2}$, $c = 8a_c$	> 2
M	Monoclinic	$a \approx \sqrt{6}a_c$, $b \approx \sqrt{2}a_c$, $c \approx 3\sqrt{2}a_c$, $\beta \approx 125°$	≥ 2
R	Pseudocubic	$a = 6a_c$	< 2

Note. The lattice parameters and the symmetries were inferred using limited number of low-index diffraction patterns characteristic for each phase and should be considered as tentative only.

[a]Phase T is a commensurate approximant of the IC phase.

ratios in the domains of both M (1.96 ± 0.06)[7] and IC/T[8] (1.99 ± 0.07) structures: the differences in the mean Sr/Nb ratio, if any, do not exceed 5–6% which represent 2CV% (CV% refers to the coefficient of variance) for ratios measured in the two types of domains. The Sr/Nb ratio in the R phase (1.76 ± 0.06) was about 10% lower compared to both IC/T and M phases; the differences were statistically significant. Because R domains are Sr-deficient with respect to an average composition, the Sr/Nb ratio in either the IC/T or M structures (or both) must be greater than the average value of 2; that is, these phases must contain some oxygen vacancies. According to our measurements, the Sr/Nb ratios in the IC/T and M phases are in the range 2–2.15. An Sr/Nb ratio of 2.1 corresponds to $Sr(Sr_{0.35}Nb_{0.65})O_{2.9}$ stoichiometry with the 0.8 oxygen vacancies per a double-perovskite unit cell ($V = 8a_c^3$).

The IC and T phases exhibit a modulation defined by a vector $\mathbf{q} = (1/4 - z)\langle 221\rangle_c^*$, with $z \approx 0.009$ and $z = 0$ resulting in the incommensurate structure, IC, and its commensurate approximate, T, respectively. The modulation produces satellites around each of the fundamental reflections; in the $\{110\}_c$ reciprocal lattice section of the IC structure, the satellites form wavy rows along the $\langle 001\rangle_c$ direction (Figs. 11a and 12a). If this superstructure were commensurate, the satellites would be located on the straight lines parallel to $[001]_c$. Indeed, some domains feature such a commensurate superstructure (Fig. 12c), T, with a pseudo-tetragonal unit cell and lattice parameters $a = 2a_c\sqrt{2}$, $b = 2a_c\sqrt{2}$ and $c = 8a_c$. The volume fraction of the commensurate domains apparently was small as they did not produce any significant contribution to the selected area electron diffraction patterns.

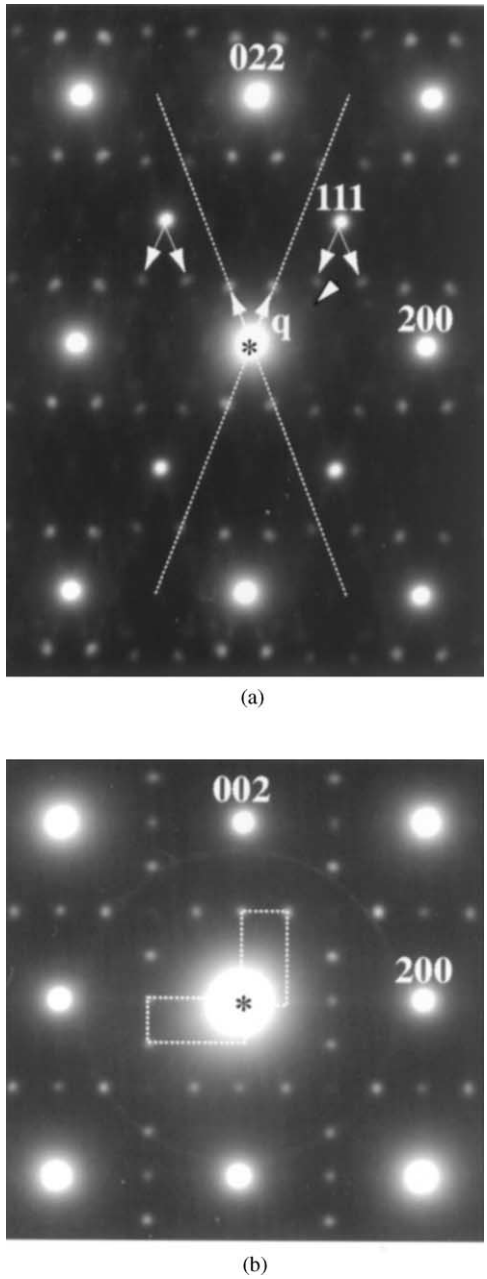

FIG. 11. SAD diffraction patterns recorded from the 900°C-annealed $Sr_4Nb_2O_9$ specimen. The fundamental reflections are indexed according to the $Fm\bar{3}m$ structure with $a = 2a_c$. (a) In the $\langle 110\rangle_c$ orientation, the satellites flanking all fundamental reflections are observed at the incommensurate $\mathbf{q} = (1/4 - z)\langle 221\rangle$ positions. (Very weak reflections, such as that indicated by the black arrow, correspond to the domains of a different type described in Fig. 14.) (b) The $\langle 001\rangle_c$ zone axis pattern from the same area features a commensurate doubling of periodicity along one of the cubic axis, that is, $a = 4a_c$ along that direction. Two crystallographic variants contribute to the pattern.

[7]The uncertainties represent single standard deviation, 1σ, estimated from 6–8 measurements (points).

[8]Since both IC and T phases exhibit very similar structures (the T phase is a commensurate approximant of the IC phase), and their domains coexist in the intimate mixture, these phases were considered identical for the compositional analysis and denoted as IC/T.

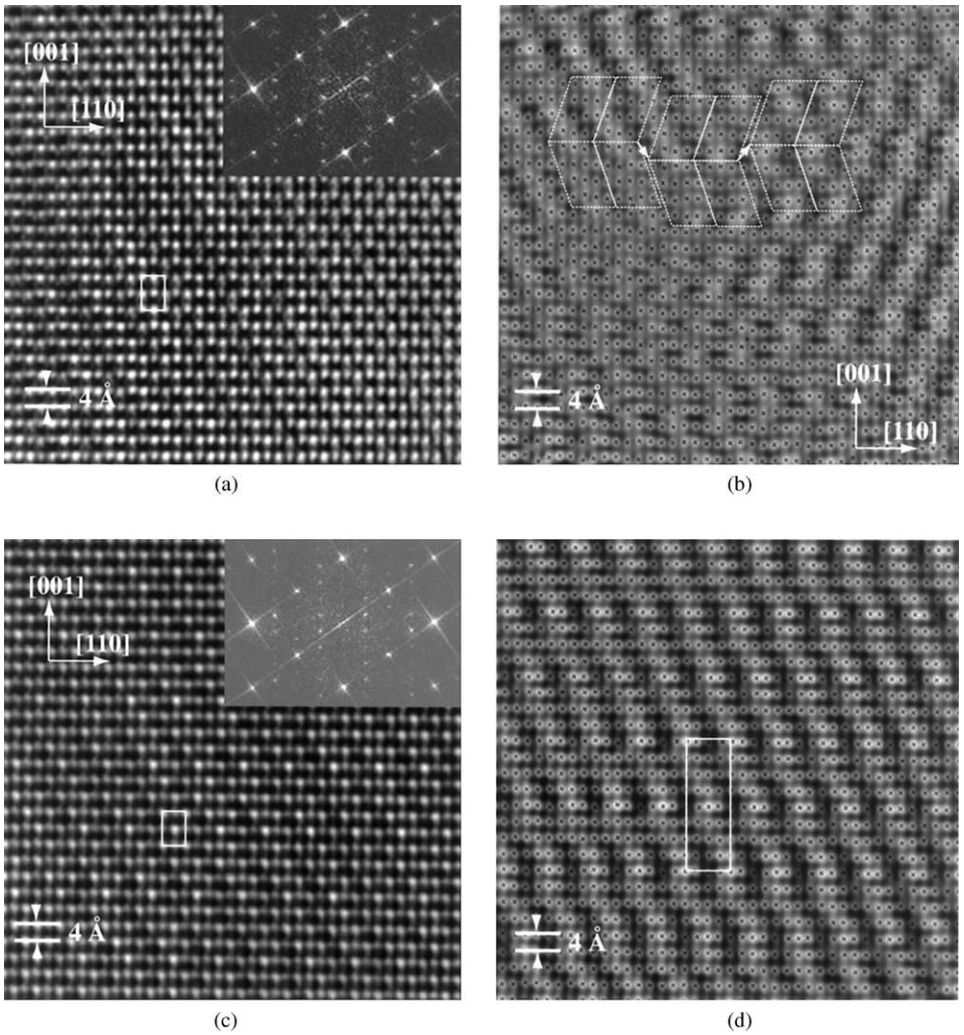

FIG. 12. (a) Structural image of the single IC domain along the $\langle 110\rangle_c$ direction. The corresponding FFT transform (inset) features incommensurate satellites at $\mathbf{q} = (1/4\text{-}z)\langle 221\rangle_c$ positions. The average contrast in the unprocessed image matches a double-perovskite periodicity. (b) The same image as shown in (a) but Fourier-filtered using incommensurate satellites and four fundamental reflections (weighted by a factor $w = 0.15$). The contribution of the modulation into the contrast is drastically enchanced in the filtered image. The basic unit, which describes the correlations in the contrast, is outlined by the parallelogram. Apparently, the incommensurate periodicity is caused by the faults in the stacking of these units which occur on the $\{221\}_c$ planes with an average periodicity between $4d_{221}$ and $5d_{221}$; the faults occur on both the $(221)_c$ and $(22\bar{1})_c$ planes. (c) Structural image of another domain in the same grain which features similar satellites as observed in (a) but located at commensurate $1/4[221]^*_c$ positions. (d) The same image as shown in (c) but Fourier-filtered using both the superlattice and the fundamental ($w = 0.15$) reflections. The contrast can be described by a stacking of the same basic units as identified in (b), but without stacking faults. The resulting periodicity in the image is $8a_c \times 2a_c\sqrt{2}$. This superlattice, denoted as T, apparently represents a commensurate approximant of the IC structure.

Phase contrast images of the IC and T phases (Figs. 12b and 12d), Fourier filtered using both incommensurate/superlattice and fundamental ($w = 0.15$) reflections, indicated that the incommensurate periodicity is caused by the stacking-fault-like defects which occur on the $\{221\}_c$ planes with the average periodicity between $4d_{221}$ and $5d_{221}$. The $(110)_c$ projection of the displacement vector for these defects is $R = \langle 221\rangle_c$, which corresponds to a lattice vector $\langle 110\rangle_c$.

Diffraction patterns from the IC/T domains in the $\langle 001\rangle$ orientation (Fig. 11b) exhibit $4a_c \times 2a_c$ periodicity; the reflections with $k + 1 \neq 2n$ are extinct (Fig. 11b). Superlattice reflections in the orientation appear commensurate and reflect periodicity of the monoclinic basic unit outlined in Fig. 12. The average phase contrast in the corresponding structural images (Fig. 13a) fits that of a simple perovskite; the relative contribution of a superstructure to the images is apparently very weak. In this image, the brightest spots represent B-cation columns and the dark spots correspond to the oxygen columns. The contribution of superstructure was drastically enhanced by Fourier filtering using both

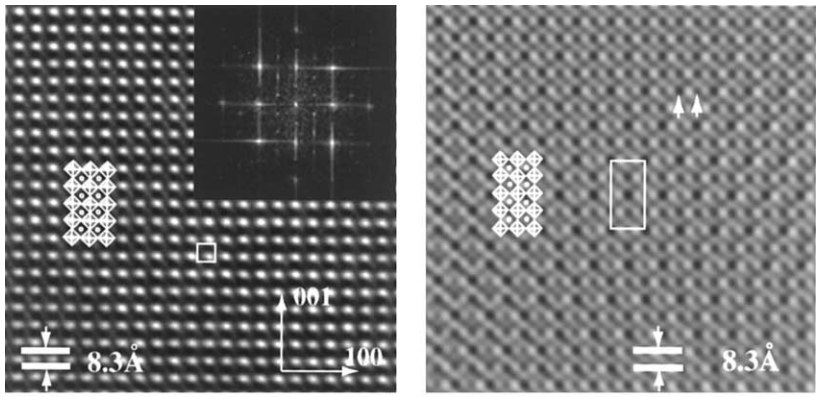

FIG. 13. (a) Phase contrast image of a single IC domain in the $\langle 001 \rangle_c$ orientation. The corresponding Fourier transform is shown as an inset. The average contrast features $2a_c \times 2a_c$ periodicity. According to image simulations, the bright spots correspond to the cation columns. (b) The same image Fourier-filtered using superlattice and fundamental reflections ($w = 0.2$). The superlattice $4a_c \times 2a_c$ periodicity is evident and outlined by the rectangle. The assumed correspondence between the contrast and the structural projection is indicated in the image. Note the difference in intensity of black spots indicated by the arrows. We interpret these black spots as representing oxygen columns.

superlattice and fundamental ($w = 0.15$) reflections (Fig. 13b). The modulation of contrast intensity among the bright spots is consistent with B-site ordering. However, a clear asymmetry of intensity of dark spots (indicated by arrows) is observed around the B sites (Fig. 13b). Similar phase contrast modulation was previously reported by Caldes *et al.* (18) for the $Sr(Sr_{0.4}Ta_{0.6})O_{2.9}$ compound, having the same superstructure periodicity in the $\langle 001 \rangle_c$ orientation. The contrast has been attributed to the mixed B1-site ordering coupled to the ordering of oxygen vacancies. This interpretation also provides a plausible explanation for the contrast presently observed. Thus, the IC and T phases were assumed to feature a combination of B-cation and oxygen vacancy ordering, which are most likely responsible for the incommensurate nature of the IC structure. The presence of oxygen vacancies in these phases is supported by the results of compositional analysis.

The M superstructure (Figs. 14 and 15) has an apparent monoclinic symmetry with approximate lattice parameters $a \approx a_c\sqrt{6}$, $b \approx a_c\sqrt{2}$, $c \approx 3a_c\sqrt{2}$ and $\beta \approx 125°$. The unit cell is metrically similar to that observed for the $P2_1/c$ Ca $(Ca_{1/3}Nb_{2/3})O_3$ polymorph (9, 10) with a combination of 2:1 B-cation ordering and $a^+b^-b^-$ octahedral tilting. However, M differs from the $Ca(Ca_{1/3}Nb_{2/3})O_3$ polymorph by the presence of strong $\mathbf{k} = 1/2[111]^*_c$ reflections in the direction parallel to the $\mathbf{k} = 1/6[111]^*_c$ vector. The observed reflection conditions indicate that the symmetry of M is $P2_1$ or lower. Assuming $Sr_4Nb_2O_9$ stoichiometry, the observed electron diffraction patterns can be accounted for by a sequence $\{SrNb(Sr_{1\,2}/Nb_{1/2})Nb(Sr_{1/2}/Nb_{1/2})Nb \ldots\}$ of $\{111\}^*_c$ B-cation planes, where round brackets denote mixed Sr/Nb layers. This sequence, produced by a partial ordering on the random B sites of the 1:1 ordered structure, results in a trigonal superlattice. The observed monoclinic unit cell can be accounted for by the presence of octahedral tilting (e.g., $a^+b^-b^-$, similar to $Ca_4Nb_2O_9$). The proposed $\mathbf{k} = 1/6[111]^*_c$ ordering provides a compromise between the trend to complete segregation of Sr and Nb cations onto different $\{111\}_c$ planes, and increasing average distortion of the B2 = Nb environment associated with such cation rearrangements. In that sense, the M superstructure is similar to the metastable $Ca_4Nb_2O_9$ polymorph with the

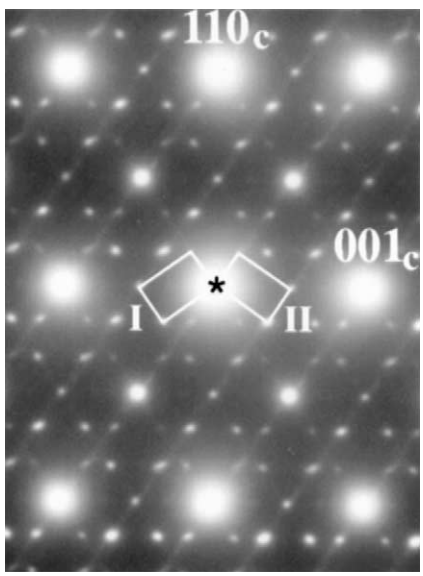

FIG. 14. Representative SAD diffraction pattern recorded from the M phase in the 900°C-annealed $Sr_4Nb_2O_9$ specimen. The fundamental reflections are indexed according to the $Fm\bar{3}m$ structure with $a \approx 2a_c$. Superlattice reflections represent two crystallographic variants of the M structure with the ordering vectors $\mathbf{k}_1 = 1/6[111]^*_c$ and $\mathbf{k}_2 = 1/6[11\bar{1}]^*_c$, respectively. Diffraction patterns of this phase were attributed to a monoclinic structure with lattice parameters $a = \sqrt{6}a_c$, $b \approx \sqrt{2}a_c$, $c \approx 3\sqrt{2}a_c$ and $\beta \approx 125°$.

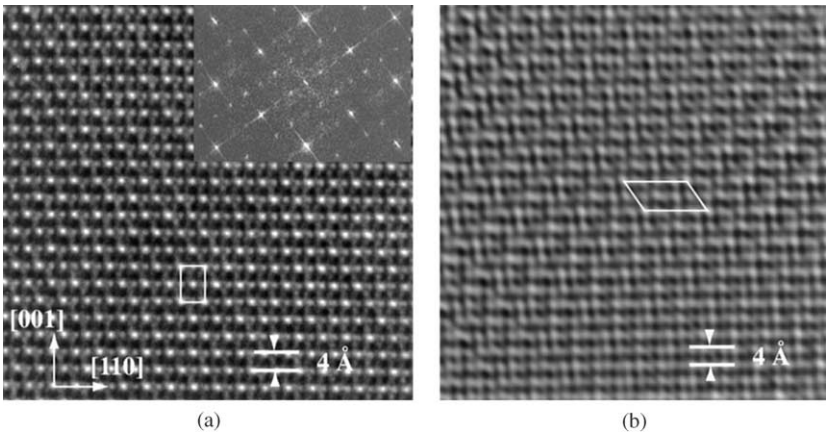

FIG. 15. (a) Structural image of the single M-phase domain in the $\langle 110 \rangle$ orientation. The corresponding FFT pattern is shown as an inset. (b) The same image Fourier-filtered using both superlattice and fundamental reflections ($w = 0.2$). The contrast modulation due to a superstructure is clearly visible in the filtered image.

$\mathbf{k} = 1/4[111]^*_c$ ordering of Ca and Nb on the B sites. For the same stoichiometry, the ordering vector $\mathbf{k} = 1/6[111]^*_c$ provides a smaller average distortion of the Nb environment than the $\mathbf{k} = 1/4[111]^*_c$ ordering, consistent with the larger size difference of Sr and Nb.

The fourth superstructure, R, identified in the same specimen, produced diffraction patterns (Fig. 16) and phase contrast (Fig. 17) strikingly similar to those observed for the compound "$Ca_3Nb_2O_8$" (25) (I. Levin, unpublished results). Vanderah *et al.* reported this compound to occur at the composition $Ca_{3.403}Nb_{2.239}O_9$ (26). The "$Ca_3Nb_2O_8$" structure was initially described by the pseudocubic F-centered unit cell with $a = 6a_c$. According to preliminary results obtained by Grey *et al.* (26), this compound crystallizes with a perovskite-like structure with an apparent $R3$ (or lower) symmetry and features a combination of ordered Ca vacancies on the A sites, B-site ordering and octahedral tilting. The B-site ordering in $Ca_3Nb_2O_8$ can be described as a derivative of the 1:1 ordered structure with additional ordering of Ca and Nb on the mixed B1 sites in the $\{111\}$ cation planes (26). The present observations suggest formation of a similar "$Sr_3Nb_2O_8$"-like structure which, reportedly (17), does not form as a stable compound. The similarity to the "$Ca_3Nb_2O_8$" compound, where some of the A sites remain vacant, is consistent with the Sr deficiency (compared to $Sr_4Nb_2O_9$) of the R structure identified by the compositional analysis; nevertheless, the Sr/Nb ratio in the R phase appears to be higher than that expected for $Sr_3Nb_2O_8$ stoichiometry.

3.4. Relationship between the HT — and 900°C — Annealed Specimens

The relationship between the HT-$Sr_4Nb_2O_9$ and the 900°C-annealed specimens is evident from Fig. 18, which shows a $\langle 110 \rangle_c$ electron diffraction pattern, recorded from the area that contains both IC and M phases, and superimposed onto the $\langle 110 \rangle_c$ pattern from the HT specimen. Superlattice reflections in the diffraction patterns of the annealed specimen are coincident with the positions of condensation of diffuse intensity in the HT specimen. These observations suggest that HT-$Sr_4Nb_2O_9$ specimens already contain a mixture of nanodomains representing different superstructures, which were further developed by 900°C annealing. Because these superstructures exhibit slightly different Sr/Nb ratios, the HT specimens must also exhibit compositional *heterogeneity* on the nanometer scale. Observed superstructures have distinct symmetries, and are likely to exhibit octahedral tilting of different topologies. Conceivably, averaging of both oxygen and A-cation displacements over such nanodomains produced an apparent positional disorder identified by X-ray and neutron powder diffraction for the oxygen and Sr (A-sites) ions.

The common features of various metastable phases identified in $Sr_4Nb_2O_9$ specimens is strong $\mathbf{k} = 1/2\langle 111 \rangle^*_c$ reflections along all four $\langle 111 \rangle_c$ directions, which (in the absence of octahedral tilting) indicate 1:1 ordering on the B sites. Thus, the metastable superstructures are likely related to some additional ordering on the mixed B1 sites of the 1:1 ordered array. Indeed, development of the metastable phases proceeded by relatively slow kinetics, which is consistent with B-site ordering. However, these metastable phases have different Sr/Nb ratios, and, therefore, a possibility of either A-site or oxygen vacancy ordering must also be considered. In fact, ordering of A-site vacancies, coupled to the B1-site ordering, has been proposed in the $Ca_3Nb_2O_8$ compound (26), which is believed to crystallize in a structure similar to the R phase. Additionally, the present analysis of IC/T structural images suggested a combination of B1-cation ordering with oxygen vacancy ordering. B1-site

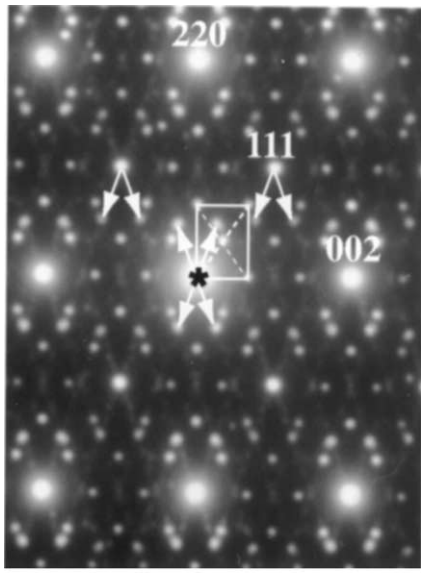

(a)

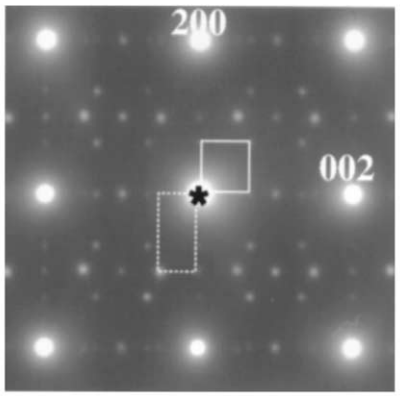

(b)

FIG. 16. SAD diffraction patterns in the [110] and [001] orientations from the area containing both the IC structure, and some other phase. In the [110] orientation, the extra reflections of this phase, denoted as R, produced a centered rectangular pattern outlined in the figure. The superlattice reflections of the R phase are identical to those observed for the compound "$Ca_3Nb_2O_8$" with pseudo-cubit F-centered unit cell and $a \approx 6a_c$.

ordering, which generates symmetrically non-equivalent oxygen sites can promote ordering of oxygen vacancies, and vice versa. In particular, oxygen vacancies are expected at the oxygen sites participating in those B1–O–B2 links, where the B1 sites are preferentially occupied by the Sr ions: such ordering would reduce an abnormally large compressive bond strain at the B1 sites. Oxygen vacancies could also explain the displacements of Sr cations on B1 sites suggested by the structural refinements of the X-ray and neutron powder diffraction data: displacements of Sr toward vacant oxygen sites would further reduce an abnormally large BVS for these cations.

The present results do not provide sufficient evidence to ascertain whether the diffuse scattering existed at $T > 1250°C$—being associated with a transition state—or, developed on cooling. However, a condensation of diffuse intensity in the superlattice reflections apparently occurred on cooling, as inferred from the domain growth upon subsequent annealing at 900°C. Conceivably, a number of metastable structures, having similar formation energies, exist at closely spaced Sr/Nb ratio values. Thus, small heterogeneties of the Sr/Nb ratio, at a nanometer scale, can lock into a mixture of different superstructures as the temperature is reduced. The metastable phases transform to the stable LT-$Sr_4Nb_2O_9$ polymorph upon annealing in the temperature range 1100–1200°C, and the transformation is irreversible.

3.5. *Raman Spectra*

Raman spectra recorded from the HT-$Sr_4Nb_2O_9$, LT-$Sr_4Nb_2O_9$ and the 900°C-annealed specimens with a mixture of metastable phases (IC, T, M, R) are summarized in Fig. 19. The Raman spectrum of HT-$Sr_4Nb_2O_9$ is similar to that presented by Choisnet *et al.* (27), and features four distinct resonance peaks at 780, ~580, ~420 and ~320 cm^{-1} (the last three peaks are broad and their locations can be determined only approximately). These four peaks are consistent with the 1:1 ordered $Fm\bar{3}m$ cubic double-perovskite structure, where the strongest 780 cm^{-1} peak is related to a 'breathing" mode of the [BO_6] oc-

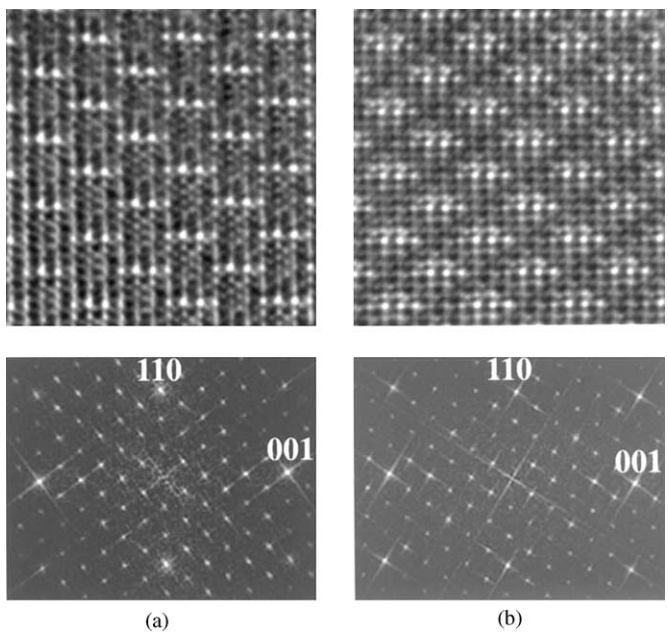

(a) (b)

FIG. 17. Structural images and the corresponding FFT patterns of the R phase and the compound "$Ca_3Nb_2O_8$". A similarity in the phase contrast is observed, suggesting that both phases exhibit similar structures.

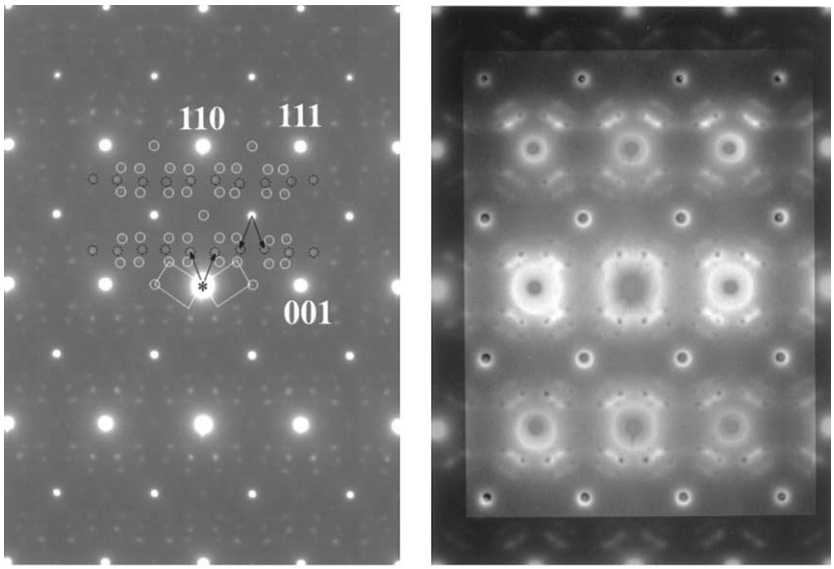

FIG. 18. (a) SAD diffraction pattern from the area containing both IC and M phases in the $\langle 110\rangle_c$ orientation; two variants of the M phase contribute to the pattern. (b) The same diffraction pattern superimposed onto the pattern recorded from the HT specimen and containing diffuse scattering. Correspondence between the locations of superlattice reflections and the diffuse intensity maxima is evident.

tahedra. The spectrum of HT-$Sr_4Nb_2O_9$ also features "shoulders" on both sides of the 780 cm^{-1} peak. The shoulders become more pronounced in the Raman spectrum of the 900°C-annealed specimen, which suggests that they are related to the metastable superstructures. Previously, development of similar shoulders was observed to accompany formation of the metastable $Ca_4Nb_2O_9$ polymorph with $\mathbf{k} = 1/4[111]^*_c$ ordering on the mixed B1 sites of the 1:1 ordered B-cation array (9). This correlation is consistent with an additional ordering on the B1 sites proposed by the structural analyses of the metastable phases in the 900°C-annealed $Sr_4Nb_2O_9$. Developed of these metastable phases is also manifested in the appearance of multiple sharp features within the broad ~580, ~420 and ~320 cm^{-1} bands. Otherwise, the spectra of both the HT and 900°C-annealed specimens are similar to each other, and dissimilar from the spectrum of the LT-$Sr_4Nb_2O_9$ phase. The difference is consistent with a distinct arrangement of the B cations (superimposed onto octahedral tilting) in the LT-$Sr_4Nb_2O_9$ phase, as compared to the common 1:1 B-cation arrangement in both the LT-$Sr_4Nb_2O_9$ and the metastable structures.

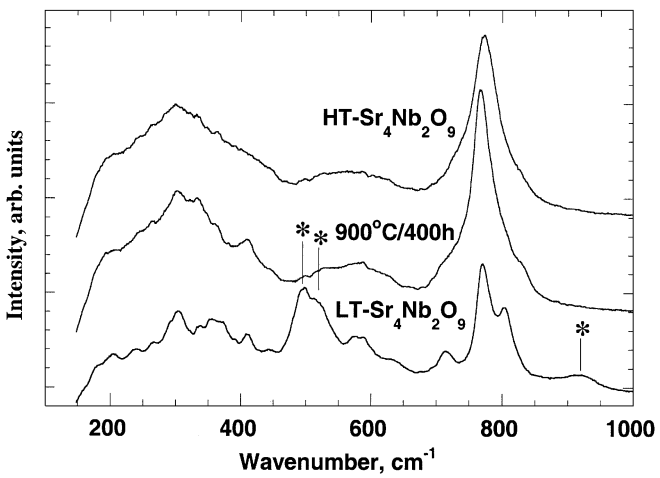

FIG. 19. Raman spectra recorded from the HT-$Sr_4Nb_2O_9$, 900°C (400 h)-annealed and LT-$Sr_4Nb_2O_9$ specimens. Peaks indicated by asterisk are related to lumenescence.

3.6. Dielectric Properties

Temperature dependencies of the dielectric constant for both the HT- and LT-$Sr_4Nb_2O_9$ specimens measured at 1 MHz are presented in Fig. 20. The HT specimen exhibits non-monotonic $\varepsilon(T)$ dependence with a maximum $\varepsilon = 40.3$ observed near $T = 0$°C. In contrast, the LT-$Sr_4Nb_2O_9$ specimen exhibits nearly linear temperature response with ε(at 25°C) = 30.7 and $\tau_\varepsilon = +113$ ppm/°C. The dielectric constant of the HT specimen is about 30% higher than that of LT-$Sr_4Nb_2O_9$. The HT specimen exhibited dielectric losses of about 2×10^{-3} (at 1 MHz), while those in LT-$Sr_4Nb_2O_9$ were at least an order of magnitude lower. Polarization measurements on both specimens did not reveal ferroelectric behavior.

Non-monotonic temperature dependence of permittivity in the HT specimen can be attributed to competitive

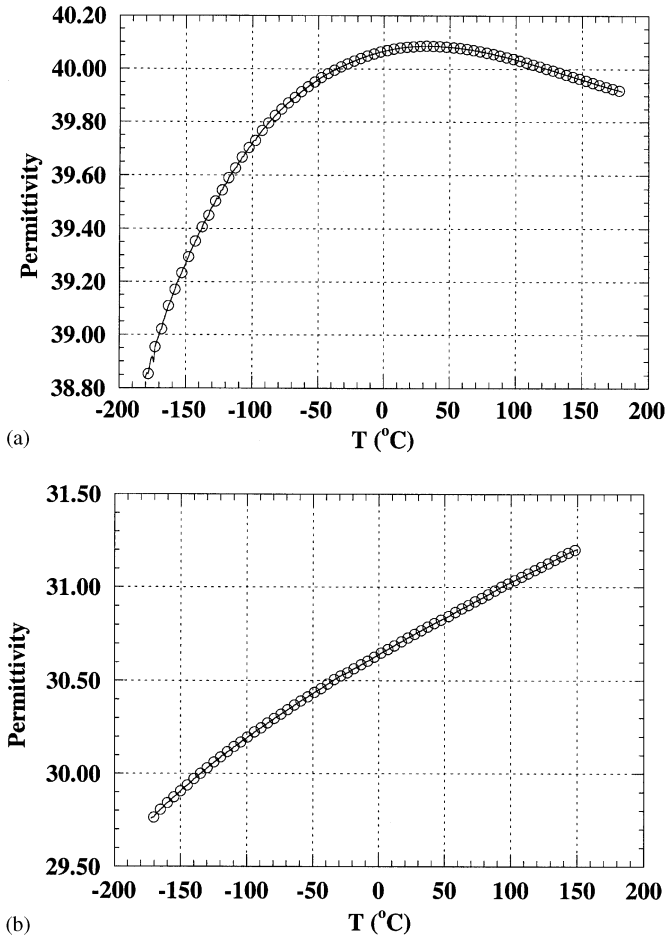

FIG. 20. Temperature dependence of relative permittivity for (a) HT-$Sr_4Nb_2O_9$ and (b) LT-$Sr_4Nb_2O_9$.

dielectric responses from the nano-sized regions with different structures and slightly different Sr/Nb ratios. The relatively high permittivity of this specimen is consistent with the less distorted cation environments typically associated with the 1:1 partially ordered B-cation arrays as compared to the completely ordered structures with $A(B'_{1/3}B''_{2/3})O_3$ stoichiometry (10, 28). An order of magnitude decrease in dielectric loss on going from HT- to LT-$Sr_4Nb_2O_9$ specimens correlates with a large decrease in permittivity.

4. CONCLUSIONS

Two thermodynamically stable polymorphs of $Sr_4Nb_2O_9$ were confirmed to occur above and below 1250°C. The high-temperature polymorph, HT-$Sr_4Nb_2O_9$, exhibits an average cryolite-like structure ($Fm\bar{3}m$, $a = 2a_c$) with NaCl-like (1:1) ordering of Sr and Nb on the B sites. The low-temperature polymorph has apparent $P2_1/n$ monoclinic symmetry ($a \approx 6a_c\sqrt{3}$, $b \approx 2a_c\sqrt{2}$, $c \approx a_c\sqrt{6}$, $\beta \approx 90°$C), and features a different but undetermined type of B-site ordering. Electron diffraction studies of HT specimens revealed diffuse intensity contours which were consistent with local ordering on the mixed Sr/Nb sites of the 1:1 ordered B-cation array. Concentration of intensity at certain points within the diffuse intensity contours was observed and attributed to the presence of superstructure nanodomains. Structural refinements using neutron powder diffraction data indicate that the HT specimens also exhibit local displacements of oxygen atoms which resemble octahedral tilting. The diffuse scattering developed into arrays of sharp superlattice reflections after annealing the HT specimen at 900°C. The reflections correspond to four distinct metastable superstructures derived from the 1:1 ordered B-cation array. These phases exhibit different Sr/Nb ratios and, therefore, are not true polymorphs of $Sr_4Nb_2O_9$. Their structures were attributed to additional ordering of Sr and Nb on the random $B' = (Sr_{2/3}Nb_{1/3})$ sites, combined with ordering of either A-site or oxygen vacancies (depending on the Sr/Nb ratio in a particular phase). The metastable structures undergo irreversible transformation to the stable LT-$Sr_4Nb_2O_9$ polymorph upon annealing at 1100–1200°C. Comparison of diffraction patterns from the HT and 900°C-annealed specimens indicated that nanodomains of at least two of the four metastable phases were present in the HT specimen. The high-temperature phase exhibits a relative permittivity of 40 with a non-linear temperature dependence that was attributed to the competitive dielectric responses of nanodomains representing different superstructures with distinct Sr/Nb ratios. The LT-$Sr_4Nb_2O_9$ polymorph has a relative permittivity of 30 with near-linear temperature dependence. The difference in permittivities of the two polymorphs was ascribed to a larger distortion of the B-cation environments in the completely ordered LT-$Sr_4Nb_2O_9$ structure. The structural behavior of $Sr_4Nb_2O_9$ differs remarkably from that of the $Ca_4Nb_2O_9$: none of the low-temperature superstructures of $Sr_4Nb_2O_9$ were observed in $Ca_4Nb_2O_9$, and vice versa. The high-temperature polymorphs of the two compounds feature similar 1:1 ordered B-cation arrangements, but differ by the absence of octahedral tilting in HT-$Sr_4Nb_2O_9$, as opposed to the strong $a^+b^-b^-$ octahedral tilting in HT-$Ca_4Nb_2O_9$.

ACKNOWLEDGMENTS

The assistance of J. P. Cline and B. A. Reisner with diffraction experiments is greatly appreciated.

REFERENCES

1. L. E. Cross, *Ferroelectrics* **76**(3–4), 241–267 (1987).
2. W. Wersing, *Curr. Opin. Solid State Mater.* **1**(5), 715–731 (1996).
3. P. K. Davies, J. Z. Tong, and T. Negas, *J. Am Ceram. Soc.* **80**(7), 1727–1740 (1997).

4. J. Lecomte, J. P. Loup, M. Hervieu, and B. Raveau, *Phys. Stat. Sol. A* **65,** 743–752 (1981).
5. A. S. Nowick and Y. Du, *Solid State Ionics* **77,** 137 (1995).
6. R. Glöckner, A. Neiman, Y. Larring, and T. Norby, *Solid State Ionics* **125,** 369–376 (1999).
7. P. K. Davies, *Curr. Opin. Solid State Mater.* **4**(5), 467–471 (1999).
8. E. L. Colla, I. .M. Reaney, and N. Setter, *J. Appl. Phys.* **74**(5), 3414–3425 (1993).
9. I. Levin, J. Y. Chan, R. G. Geyer, J. E. Maslar, and T. A. Vanderah, *J. Solid State Chem.* **156,** 122–134 (2001).
10. I. Levin, L. A. Bendersky, J. P. Cline, R. S. Roth, and T. A. Vanderah, *J. Solid State Chem.* **150,** 43–61 (2000).
11. M. Hervieu, B. Raveau, J. Lecomte, and J. P. Loup, *Rev. Chim. Miner.* **22,** 44–57 (1985).
12. D. Pasero and R. J. D. Tilley, *Res. Chem. Intermediat.* **25**(2), 229–242 (1999).
13. M. Hervieu, B. Raveau, J. Lecomte, and J. P. Loup, *Chem. Scr.* **25**(3), 206–211 (1985).
14. P. A. Stadelmann, *Ultramicroscopy* **21,** 131–146 (1987).
15. G. Cliff and G. W. Lorimer, *J. Microsc.* **103,** 203 (1975).
16. A. C. Larson and R. B. Von Dreele, "General Structure Analysis System." Los Alamos National Laboratory Report LAUR 86-748, 1994.
17. J. Y. Chan, I. Levin, T. A. Vanderah, R. G. Geyer, and R. S. Roth, Subsolidus phase relations and dielectric properties in the $SrO–Al_2O_3–Nb_2O_5$ system. *Int. J. Inorg. Mater.* **2,** 107–114 (2001).
18. M. T. Caldes, P. Deniard, X. D. Zou, R. Marchand, N. Diot, and R. Brec, *Micron* **32,** 497–507 (2001).
19. R. D. Shannon, *Acta Crystallogr. A* **32,** 751 (1976).
20. I. D. Brown and D. Altermatt, *Acta Crystallogr. B* **41,** 244–247 (1985).
21. R. De Ridder, G. van Tendeloo, D. van Dyck, and S. Amelinckx, *Phys. Stat. Sol. A* **38,** 633–674 (1976).
22. M. Sauvage and E. Parthe, *Acta Crystallogr. A* **30,** 239–246 (1974).
23. M. Brunel, F. De Bergevin, and M. Conrad, *J. Phys. Chem. Solids* **33,** 1927–1941 (1972).
24. J. Billingham, P. S. Bell, and M. H. Lewis, *Acta Crystallogr. A* **28,** 602–606 (1972).
25. T. A. Vanderah, W. Febo, J. Y. Chan, R. S. Roth, J. M. Loezos, L. D. Rotter, R. G. Geyer, and D. B. Minor, *J. Solid State Chem.* **155,** 78–85 (2000).
26. I. A. Grey, L. Cranswick, and R. S. Roth, to be published.
27. J. Choisnet, M. Hervieu, and B. Raveau, *Rev. Chim. Miner.* **17,** 118–130 (1980).
28. J. Takahashi, T. Fujii, S. Shimada, and K. Kodaira, *J. Eur. Ceram. Soc.* **19,** 1089–1093 (1999).